

# Journal of Geophysical Research: Atmospheres

## RESEARCH ARTICLE

10.1002/2017JD027240

**Key Points:**

- Satellite observations are used to explore relationships between changes in NH maritime extratropical cyclones (ETCs) aerosol optical depth (AOD) and in cloud cover
- ETCs with large AOD exhibit larger middle- and high-level cloud cover, and smaller low-level cloud cover, relative to low AOD ETCs
- Column water vapor and ascent strength impact the observed relationship between AOD and cloud cover in ETCs

**Correspondence to:**C. M. Naud,  
cn2140@columbia.edu**Citation:**

Naud, C. M., Posselt, D. J., & van den Heever, S. C. (2017). Observed covariations of aerosol optical depth and cloud cover in extratropical cyclones. *Journal of Geophysical Research: Atmospheres*, 122, 10,338–10,356. <https://doi.org/10.1002/2017JD027240>

Received 2 JUN 2017

Accepted 12 SEP 2017

Accepted article online 15 SEP 2017

Published online 5 OCT 2017

## Observed Covariations of Aerosol Optical Depth and Cloud Cover in Extratropical Cyclones

Catherine M. Naud<sup>1</sup> , Derek J. Posselt<sup>2</sup>, and Susan C. van den Heever<sup>3</sup><sup>1</sup>NASA-GISS, Columbia University, New York, NY, USA, <sup>2</sup>Jet Propulsion Laboratory, California Institute of Technology, Pasadena, CA, USA, <sup>3</sup>Department of Atmospheric Science, Colorado State University, Fort Collins, CO, USA

**Abstract** Using NASA Moderate Resolution Imaging Spectroradiometer aerosol optical depth and total cloud cover retrievals, CloudSat-CALIPSO cloud profiles, and a database of extratropical cyclones and frontal boundary locations, relationships between changes in aerosol optical depth and cloud cover in extratropical cyclones occurring over Northern Hemisphere oceans are examined. A reanalysis data set is used to constrain column water vapor and ascent strength in the cyclones in an attempt to distinguish their impact on cloud cover from the effect of changes in aerosol loading. The results suggest that high aerosol optical depth cyclones exhibit larger middle- and high-level cloud cover than their low aerosol optical depth counterparts. However, the opposite behavior is found for low-level cloud cover. These relationships are found to depend on the large-scale environment, in particular the column water vapor and vertical motion. Despite the inability of the observations to provide a causal physical link between aerosol load and cloud cover, these results can help to constrain and evaluate model simulations.

### 1. Introduction

As the main purveyors of precipitation in the midlatitudes (Catto et al., 2012) and because of the large radiative impact of their cloud fields (e.g., Haynes et al., 2011; Tselioudis et al., 2000), extratropical cyclones (ETCs) have been the object of intense scrutiny for their evolution in a changing climate (e.g., Bengtsson et al., 2009; Catto et al., 2011; Li et al., 2014; Yetella & Kay, 2016). In particular, it has been found that cloud and precipitation in ETCs are strongly dependent on both moisture amounts and cyclone strength (Field & Wood, 2007; Pfahl & Sprenger, 2016), which are expected to change. However, the impact of aerosols on ETCs, which could potentially impact clouds and precipitation, as well as the cyclones' dynamics through latent heating, is still under investigation (e.g., Fromm et al., 2016; Igel et al., 2013; Joos et al., 2017; Wang et al., 2014). For example, there is mounting evidence of a link between Asian pollution outflow and the intensification of the north Pacific storm track in winter (Wang, Zhang et al., 2014; Zhang et al., 2007) through the invigoration of the cyclones (Wang, Wang, et al., 2014). Furthermore, cloud-resolving modeling studies of aerosol impacts on warm frontal clouds and precipitation processes have demonstrated that enhanced aerosol loading appears to significantly impact the microphysical processes and structure of warm frontal systems, including the distribution of precipitation around the surface frontal boundary. The accumulated surface precipitation is affected to a much lesser extent, as a result of microphysical buffering processes (Igel et al., 2013).

Most of the prior research on this topic has been conducted using regional, mesoscale, or high-resolution process models, as observations do not allow for a clear distinction between cause and effect (e.g., Rosenfeld et al., 2014). However, even high-resolution model simulations rely on various microphysical and aerosol assumptions to some degree and therefore need to be constrained and validated with observations. Here we explore the relationships between changes in aerosol optical depth (AOD) and changes in cloud cover within extratropical cyclones using colocated A-train observations in order both to analyze the changes of ETCs developing within clean and polluted environments and to provide the data sets necessary to constrain and evaluate mesoscale through global models.

In Naud, Posselt et al. (2016), we explored Moderate Resolution Imaging Spectroradiometer (MODIS; Salomonson et al., 1989) aerosol optical depth seasonal and spatial distributions around extratropical cyclones. This work demonstrated that, because of the location of the storm tracks in the Atlantic and Pacific Oceans and their position with respect to aerosol source regions, oceanic cyclones tend to have lower AODs in winter and fall than spring and summer and tend to have larger AODs at low than high latitude. Within a 2,500 km radius centered on the low pressure point of the cyclones, relatively larger AODs were

found on average in an area corresponding to the warm frontal region and in the postcold frontal region. This spatial distribution was similar for all seasons, whether we included the regions north or 50°N or not and whether we included regions where cloud cover exceeded 80% or not. Here we use MODIS aerosol optical depth and cloud cover and combined CloudSat radar (Stephens et al., 2002) and CALIPSO lidar (Winker et al., 2009) cloud vertical profiles to explore changes in cloud cover as a function of changes in the mean cyclone-wide AOD in a large database of observed cyclones.

There are a number of potential obstacles to achieving this goal, that is, examining covariations of cloud cover and AOD in extratropical cyclones that we note at the outset of this paper. AODs retrievals are limited to cloud-free areas. As such, the observations provide no information on the aerosol content below, above, or within clouds. Consequently, the covariations in total cloud cover and AOD observed here cannot be associated to known cloud-aerosol interaction processes with the observations at our disposal. This said, our previous analysis revealed that the lack of aerosol data in cloudy regions had no effect on the spatial distribution of AODs around fronts and cyclones (Naud, Posselt et al., 2016). Therefore, our study relies on the assumption that cyclones that evolve in environments with heavy aerosol loads are likely to contain larger aerosol concentrations than cyclones evolving in clean environments despite the occurrence of precipitation and wet scavenging. Independent of cause-effect considerations, our analysis allows us to examine the relations between environmental aerosol loading and cyclone cloud cover in a climatological sense and also provides a useful constraint for model evaluation.

To ensure robust AOD samples in the near-storm environment, we average together multiple events using a compositing technique (e.g., Bauer & Del Genio, 2006; Field & Wood, 2007; Lau & Crane, 1995; Naud et al., 2006, 2012; Naud, Posselt et al., 2016), in which we analyze cyclone-centered mean quantities. Cyclone-centered composites tend to smooth out frontal structures, rendering the distinction of warm and cold air sectors difficult. Therefore, we also examine front-centered composites of cloud vertical transects (Naud et al., 2010, 2012, 2015). As we have noted previously, the cyclones with the largest AODs tend to be found in areas with large amounts of column water vapor, compared to relatively dry low AOD areas (Naud, Posselt et al., 2016). Moisture changes between high and low AOD cyclones therefore need to be taken into account, as moisture and cloud cover are strongly related. To characterize cyclone-wide water vapor content and dynamics, we use precipitable water (PW) and 500 hPa vertical velocity ( $\omega$ ) from the second version of the Modern Era Reanalysis for Research Applications (MERRA-2; Gelaro et al., 2017).

In the rest of the manuscript, we examine how changes in cyclone AOD relate to changes in cloud cover while constraining accompanying changes in PW and ascent strength. Our goal is to use this approach to isolate changes in cloud cover that might be related to changes in aerosol optical depth.

## 2. Data and Methods

For this study, the main observational data sets consist of daily NASA-Aqua MODIS and a combination of the CloudSat radar and the CALIPSO lidar. Although the Aqua platform was launched in 2002, the MODIS observations used here cover the period 2006 to 2016, to coincide with the beginning of the CloudSat and CALIPSO missions (both launched in 2006). Because of a CloudSat battery anomaly, the combined CloudSat-CALIPSO products are not available for most of 2011 and only during the daytime from July 2012 onward. In addition, as of the time of this study, data were only available through January 2016. The daytime-only availability of CloudSat after 2012 is not an issue for this study because aerosol optical depths are only retrieved during the daytime, and hence, we only sample cyclones that occur in the daytime.

Because aerosol and cloud property retrievals strongly depend on the surface type, to avoid the impact of surface changes (i.e., from ocean to land), we restrict our study to midlatitude oceans (30°–60°N). Finally, as aerosol loads are much greater in the Northern than Southern Hemisphere and of a different nature, we further limit the study to the Northern Hemisphere. A study specifically focused on the Southern Oceans will be conducted separately.

### 2.1. Extratropical Cyclones and Fronts

The extratropical cyclone locations are obtained from the NASA Modeling, Analysis, and Prediction Climatology of Midlatitude Storminess database (MCMS; Bauer & Del Genio, 2006; Bauer et al., 2016), which identifies and tracks cyclones using ERA-interim (Dee et al., 2011) 6-hourly sea level pressure fields. This

method compares well with other trackers (Bauer et al., 2016; Neu et al., 2013). Here we use the 6-hourly locations of the cyclone centers, regardless of their position along the track. This implies that a given system that evolves over multiple days will be sampled multiple times. Hereafter all 6-hourly snapshots are considered independent from one another and are referred to as an extratropical cyclone, or cyclone for short, even though some of these snapshots will be from the same storm system.

The cold and warm frontal boundaries are obtained using temperature and wind fields from MERRA-2 following a method described in Naud et al. (2010, 2015). The relatively high  $0.5^\circ \times 0.67^\circ$  spatial resolution of MERRA-2 allows for a more precise identification of frontal boundaries than other reanalyses' relatively coarser resolution. To summarize, the warm fronts are detected with the Hewson (1998) temperature gradient method using MERRA-2 potential temperatures at 850 hPa. The cold fronts are detected with the same method, as well as with the method of Simmonds et al. (2012) that measures the change in MERRA-2 surface wind direction and speed at the cold frontal boundary. Naud, Booth, et al. (2016) describe in great detail the method that is used to combine the two techniques and provide the best estimate of the cold front locations. Both cold and warm fronts are detected at a single level close to the surface and referred to as surface fronts.

## 2.2. Aerosol Optical Depth and Cloud Cover Data Sets

To obtain both AOD and total cloud cover (TCC), we use MODIS files of Collection 6 (i.e., the most recent version of the data processing) that contain AOD retrievals (Levy et al., 2013) and TCC retrievals (Menzel et al., 2008). These daily files contain gridded versions of the level 2 (instantaneous) products, averaged in  $1^\circ \times 1^\circ$  grid cells. Each location on Earth is observed at least once per day by MODIS thanks to its wide 2,330 km swath, so most extratropical cyclones in the database intersect with observations when using daily files. The aerosol retrievals use observed reflectances at six wavelengths in the visible and near infrared (Remer et al., 2005), and hence, retrievals are not performed at night. In addition, as in Naud, Posselt et al. (2016), we extract the AOD per tropospheric aerosol mode (Levy et al., 2003) and combine the nine possible modes into three distinct main modes: the "small particle mode" that includes the four fine modes (effective radii 0.1, 0.15, 0.2, and 0.25  $\mu\text{m}$ ), the "sea salt-like mode" that includes three maritime coarse mode particles (effective radii 1, 1.5, and 2  $\mu\text{m}$ ), and the "dust-like mode" that include another two coarse mode particles (effective radii 1.5 and 2  $\mu\text{m}$ ).

MODIS total cloud cover (also referred to as cloud fraction in the files) is obtained from the 1 km cloud mask (Ackerman et al., 2008) and is performed day and night. However, to ensure consistency between the aerosol and cloud cover information, the cloud cover used here is the daytime-only mean cloud fraction. For the 10 year period spanning 2006–2016, there are  $\sim 100,000$  cyclones over the Northern Hemisphere midlatitude daytime oceans with AOD retrievals available in the area surrounding the cyclone center. This region is approximated as a circular region, centered on the low-pressure minimum location, of 2,500 km radius. The radius is a compromise between ensuring a good sample size of AOD retrievals while restricting the area to encompass mainly the cyclone.

In addition, we collected CloudSat-CALIPSO joint product radar-lidar geometrical profile product (RL-GeoProf) also called *GEOPROF-Lidar* of the most recent R05 version (Mace & Zhang, 2014) which provides vertical profiles of cloud detection. This product provides the cloud base and top altitude of up to six cloud layers for each CloudSat footprint. We use this information to derive a cloud mask of 250 m vertical resolution (as in Naud et al., 2015, 2012). Because the radar cannot distinguish between cloud and precipitation particles, our cloud mask is in fact a hydrometeor mask. We obtained in excess of 40,000 cyclones selected above with GEOPROF-LIDAR retrievals available in a 1,500 km radius region within  $\pm 3$  h, with  $\sim 20,000$  in the cold frontal region (i.e., within  $\pm 1,000$  km of the surface front), and about  $\sim 15,000$  in the warm frontal region.

## 2.3. Cyclone-Centered and Front-Centered Compositing

The aerosol and cloud observations are first collected in a stereographic grid of  $14.4^\circ$  angular and 100 km radial resolution, centered on each cyclone's location of minimum in sea level pressure extending to 2500 km maximum radius (as first introduced in Naud et al., 2012). There are two main issues with this AOD characterization of the cyclones: no retrievals are available in cloudy areas of the cyclone, and no retrievals are performed over sea ice or at night. Figure 1 shows an example of a cyclone that occurred on 20 January 2007 in the Pacific Ocean, with a center located at  $40.27^\circ\text{N}$  and  $163.49^\circ\text{N}$ . The figure contains a

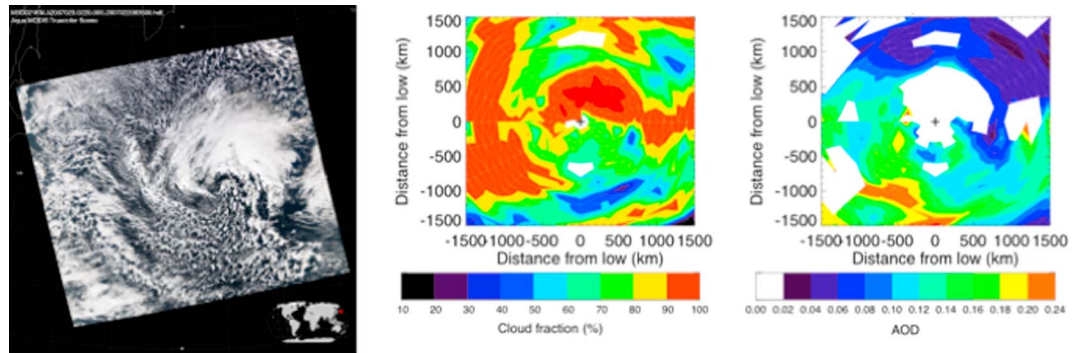


**Figure 1.** MODIS observation of an extratropical cyclone in the north Pacific Ocean that occurred on 20 January 2007 at 00:00 UT with a center located at 40.27°N and 163.49°E: (left) the MODIS Aqua true color image acquired at 2:20 UT (courtesy of [https://modis-images.gsfc.nasa.gov/IMAGES/02\\_1km\\_main.html](https://modis-images.gsfc.nasa.gov/IMAGES/02_1km_main.html)) and the corresponding cyclone-centered stereographic projection of (middle) the daytime total cloud cover and (right) the AOD. The white areas on the projections mark clear sky and areas without retrievals. The black plus indicates the location of the low-pressure center.

true color image, as well as the stereographic projections of the MODIS cloud cover and AOD. While MODIS AOD retrievals are available for a significant portion of the cyclonic region, the warm frontal region to the north and east of the center exhibits cloud fractions above 90% and is devoid of AOD retrievals. While AOD is not available in regions with cloud fraction greater than 90%, the majority of the source regions for air entering the cyclone contain AOD retrievals. Consequently, while AOD data are missing in regions with near-complete cloud cover, there are sufficient AOD data available in the cyclone vicinity to assess relationships between environmental AOD and cyclone-wide properties. To explore the effect of potential sampling issues on our analysis, we collect the number of grid cells with an AOD retrieval for each cyclone and project this number onto the stereographic grid. We do not impose any restriction on the number of grid cells available for each cyclone, but we explore retrieval availability as a function of cyclone-wide mean AOD.

We create cyclone-centered composites of various quantities, that is, we calculate the mean and/or standard deviation over multiple cyclones by superimposing the cyclone centers and stereographic grids. The quantities that are composited are the number of AOD retrievals, the mean and standard deviation of the AOD, the mean MERRA-2 precipitable water, the mean MERRA-2 500 hPa vertical velocities, and the mean MODIS total cloud cover. Figure 2 shows these composites when including all cyclones in the database, regardless of their individual characteristics. Figure 2a shows the mean AOD distribution within the cyclones. As was demonstrated in Naud, Posselt et al. (2016), there are two areas of relative maximum in AOD, one to the east of the storm center and another along the western edge. There is a relative minimum at the center, which also coincides with a small number of retrievals available (Figure 2b). Retrievals are available more often on the southern side of the low-pressure center and less often on the northern side of the cyclones, which will be more often affected by sea ice and by low illumination. Figure 2c shows that the northern side of the cyclones also displays a larger standard deviation of AOD, compared to the southern half where the AOD variability is less. The composite of total cloud cover reveals a relative minimum on the southern edge and a relative maximum at the center extending north and eastward (Figure 2d). We will refer to this area of relative maximum as the warm frontal zone (cf. Naud et al., 2012). Figure 2e shows the distribution of PW, with a sharp contrast between the humid southern half compared to the drier northern half. There is a strong correlation between the water vapor distribution and temperature in extratropical cyclone, and we will therefore refer to the southeastern quadrant where PW is relatively larger as the warm sector. The northern half of the cyclone is colder, and we will refer to it as the cold sector. Figure 2f shows the distribution of 500 hPa vertical velocities. The region of the strongest ascent coincides with the area of relatively large TCC but extends into the southeastern quadrant marking the warm conveyor belt region that is usually found in advance of the cold front. Consequently, we will refer to the southwestern quadrant, where subsidence dominates, as the postcold frontal region.

In addition, we calculate for each cyclone individually their mean cyclone-wide AOD, PW, and ascent strength (averaged only in the region of ascent, that is, where the 500 hPa vertical velocities are negative). As

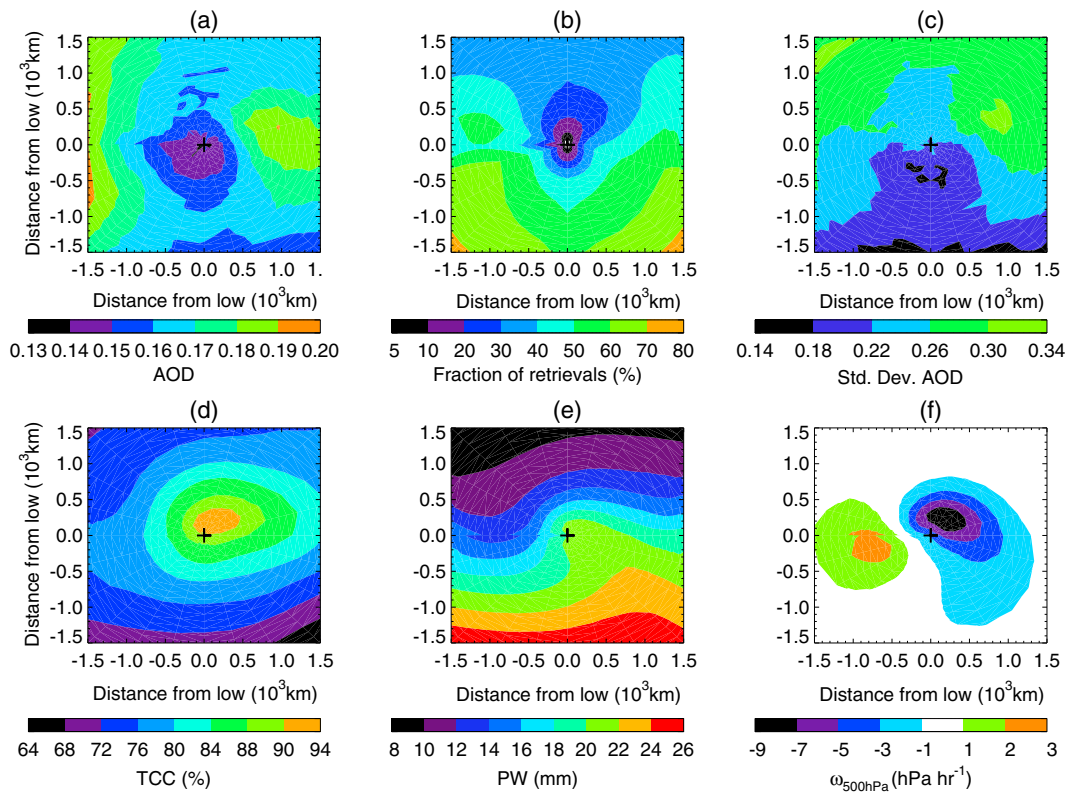


**Figure 2.** Cyclone-centered composites of (a) AOD, (b) fraction of cyclone with AOD retrievals, (c) the standard deviation of AOD, (d) total cloud cover, (e) MERRA-2 PW, and (f) MERRA-2 500 hPa vertical velocity for all NH ocean cyclones between September 2006 and August 2016.

explained above, the mean AOD is calculated for the entire 2,500 km radius region, but the mean PW and ascent strength use a circular regions of 1,500 km radius centered on the low. The size of this circular area is chosen as a compromise between including extensive cold frontal regions and excluding neighboring cyclones or anticyclones. Whether we use 1,500 km or 2,500 km radius to calculate the cyclone-wide mean AOD, we get the same results. However, by using the larger radius, we are ensuring a more robust mean with a larger number of retrievals per cyclone.

Finally, the CloudSat-CALIPSO vertical cloud mask profiles are selected if their distance to the surface front is within  $\pm 1,000$  km. Based on their distance to the front, we then place each one in a vertical grid, centered along its x axis on the surface front, of 3,000 km horizontal and 14 km vertical extent and of 100 km horizontal and 250 m vertical resolution. To build these composites, the profiles have to be available within  $\pm 3$  h and within a 2,000 km wide box centered on the surface front and of same length as the front, but the orbit needs not intersect either front. This allows for a greater sample size. The gridding method is explained in details in Naud et al. (2015). The resulting composite gives the mean frequency of occurrence of clouds along the vertical in a region perpendicular to the surface front. To provide a measure of uncertainty caused by the limited sample size, we construct composites using 400 randomly selected cold or warm fronts and calculate the difference composite between two independent subsets. We repeat this operation 100 times and use these 100 composite differences to estimate the standard deviation transects. This standard deviation is then used as a minimum allowable difference below which the composite difference between high and low AOD cyclone populations is deemed not significant.

To summarize, we obtain a database of  $\sim 100,000$  Northern Hemisphere oceanic extratropical cyclones each characterized by a mean cyclone-wide AOD, PW, and ascent strength parameter and for which we have a gridded stereographic distribution of total cloud cover and AOD and, for a smaller subset, gridded vertical distributions of cloud layer across cold and warm fronts. Next we discuss how these cyclones are sorted so that we can explore mean cyclone properties as a function of the near-cyclone mean AOD.

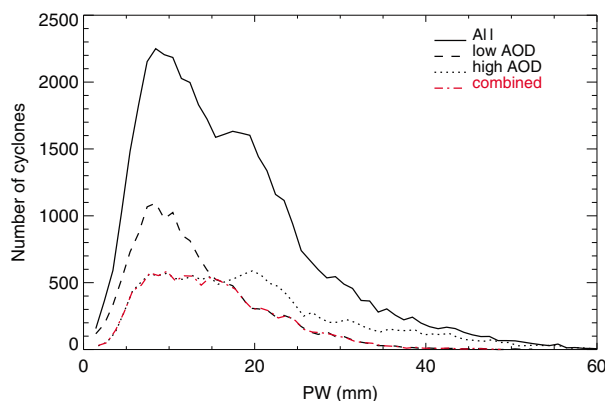


**Figure 3.** Histograms of mean cyclone-wide PW for all cyclones in the database (solid), the cyclones that fall in the low AOD category (dashed), the cyclones that fall in the high AOD category (dotted) and for a random selection of cyclones in each AOD category so that the two populations exhibit the same PW distribution (red dash dotted). The histograms are produced using 0.5 mm bins.

larger than if the same aerosol loading was observed in drier environments. We therefore need to ensure that there is very little correlation between mean cyclone-wide AOD (and cloud cover) and mean cyclone-wide PW in our data set.

As a result, in part, because in Naud et al. (2015) we find a much larger impact of moisture than ascent strength on cloud cover for the actual range of values that are observed in cyclones, we additionally constrain the AOD-based cyclone subsets such that the distribution of mean cyclone-wide PW in the high and low AOD populations is virtually identical. Figure 3 shows the distribution of mean cyclone-wide PW for the entire cyclone population, as well as for the low and high AOD cyclone populations. The histograms are obtained by sorting the mean cyclone-wide PW into 0.5 mm bins. This figure clearly shows that, while there is significant overlap between the two populations at values of PW up to 15 mm, the high AOD histogram extends to larger (wetter) PW values. There is a clear peak at approximately 8 mm PW for the low AOD population, while the high AOD population is nearly equiprobable over a range that extends from approximately 7 to 22 mm in PW. To ensure that each AOD-based cyclone population contains a similar distribution of cyclone-wide PW, we randomly select individual cyclones in each PW bin so that the number of cyclones in each bin in the low and high AOD cyclone populations is the same. This means that for the low AOD cyclones, there are fewer cyclones with mean PW less than 15 mm in the new PW-constrained low AOD cyclone population, while for the high AOD cyclones, there are fewer cyclones with mean PW above 15 mm. The resulting distribution of PW, now nearly identical in both AOD-based populations, is also plotted in Figure 3 (red line). The new AOD-based cyclone populations are reduced by about 30% when imposing this PW distribution constraint.

### 3. The Change in Extratropical Cyclone Cloud Cover Between High and Low AOD Cyclones

As explained above, we contrast cyclone composites of cloud cover between the high and low AOD cyclone populations and ensure that these two populations have similar distributions of cyclone-wide PW. Then we further constrain the cyclone population on both PW and ascent strength.

#### 3.1. Characteristics of Low Versus High AOD Cyclones With Imposed PW Distribution Constraint

Using the PW distribution-constrained high and low AOD populations, we examine the high minus low AOD composite differences of AOD, TCC, and vertical velocities, as well as the difference in the total number of available AOD retrievals (Figure 4). To estimate whether these differences are significant, we use the following method: (1) we randomly select cyclones to construct two independent subsets of 2,500 members; (2) we calculate composites for each subset of AOD, TCC, and vertical velocity and calculate the difference composite between the two cyclone subsets; and (3) we repeat the operation 100 times and then calculate the mean and standard deviation of the 100 difference composites. If the difference between the high and

#### 2.4. Conditional Sorting

To isolate the relationship between cloud cover and AOD in extratropical cyclone regions, we construct composites of cloud cover for cyclone populations defined based on their cyclone-wide mean AOD. The first step is to sort the cyclones based on their mean cyclone-wide AOD from low to large and divide them into terciles of equal population (about 30,000 cyclones per tercile). The first tercile contains cyclones with mean AOD between 0.002 and 0.12 (referred to as the low AOD cyclone population), and the third one between 0.18 and 1.4 (referred to as the high AOD cyclone population). Here we contrast these two extreme populations. However, we also need to reduce the impact of other environmental factors on both cloud and aerosols. Field and Wood (2007) found a significant correlation between cloud cover and both water vapor amount and cyclone strength. Naud, Posselet et al. (2016) also found that large AOD regions coincide with humid regions, while low AOD regions are much drier. This entails that large AOD cyclones might exhibit large cloud cover because they are more humid rather than because of a possible link between aerosols and clouds.

Also, aerosols can swell in humid environments, causing AOD to be

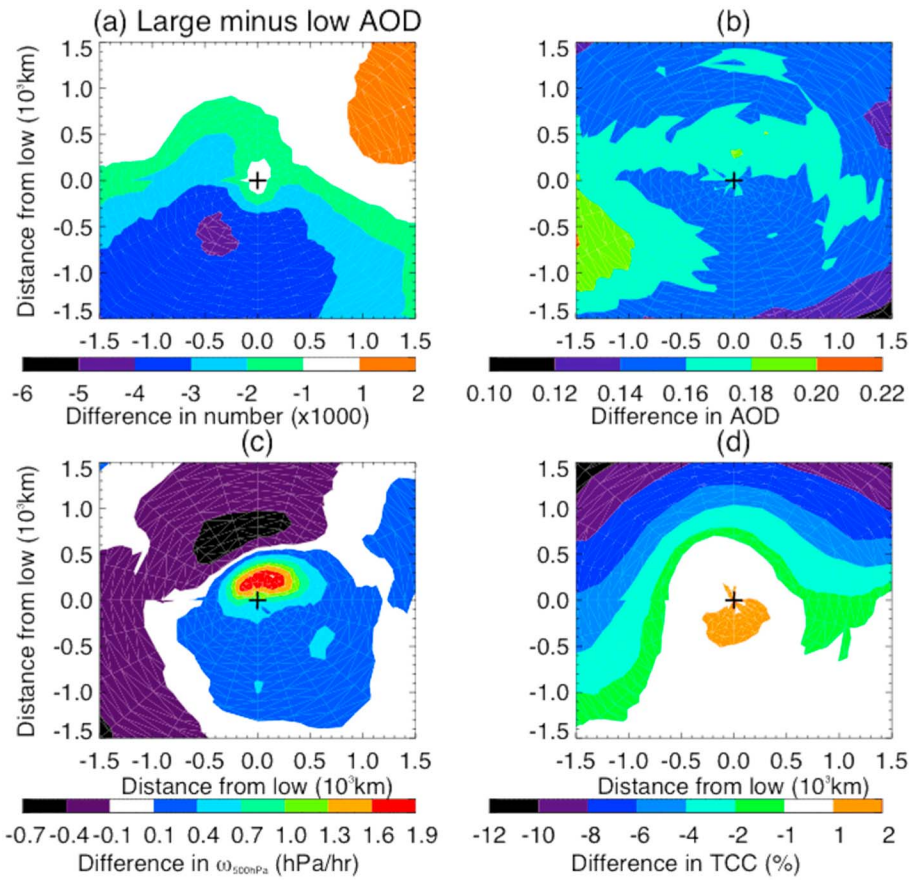


**Figure 4.** Difference in high minus low AOD populations for cyclone-centered composites of (a) number of AOD retrieval, (b) mean AOD, (c) 500 hPa vertical velocity, and (d) total cloud cover (TCC). The cyclone population is constrained to ensure similar cyclone-wide mean PW.

low AOD composites is greater (in absolute value) than this standard deviation, then the difference is deemed significant. We find, in fact, that the differences in Figure 4 largely exceed the random-based differences.

Focusing first on the composites of AOD, Figure 4a shows that for the two AOD-based cyclone populations the number of AOD retrievals are relatively similar on the polar side of the low, but that the low AOD cyclones tend to display more retrievals in the southwestern quadrant. This could be caused by slightly lower cloud cover in this part of the cyclone in low AOD cyclones. Figure 4b demonstrates that the difference in AOD between high and low AOD PW-constrained populations is at a maximum in the southwestern quadrant with a secondary maximum in the warm frontal region and warm sector and at a minimum on the equatorial edge of the southeastern quadrant. Overall, the differences to some extent follow the spatial distribution of AOD (cf. Figure 2a). Figure 4c reveals a clear difference in vertical velocity between high and low AOD PW-constrained populations: high AOD cyclones display weaker ascent to the north of the low-pressure center and slightly weaker subsidence farther north. Finally, the difference in cloud cover between high and low AOD cyclones (Figure 4d) is rather small in the warm sector and in the vicinity of the low, but high AOD cyclones display lower cloud cover in the cold sector than their low AOD counterparts. With the constraint of identical PW distributions, we find that the composites of PW are very close to one another (not shown), with differences across the cyclone area being less than 1.5 mm (compared to greater than 5 mm with the original populations).

This figure suggests that changes in the environmental AOD, and hence subsequently within the cyclones, might be linked to changes in cloud cover in the cold sector. One cause for concern remains with the difference in vertical velocities as the high AOD cyclones are weaker than the low AOD cyclones. Therefore, it is possible that any change in TCC related to changes in AOD in the warm sector might be masked by the

**Table 1**Mean Cyclone Properties for Each  $\omega$  and PW-Based Category: Number of Cyclones, PW, and  $\omega$ 

Subsets	Weak ascent ( $-4.7 < \omega < -0.72$ hPa/h)	Moderate ascent ( $-6.8 < \omega < -4.7$ hPa/h)	Strong ascent ( $-21.6 < \omega < -6.8$ hPa/h)
Low PW	11,051	11,293	12,280
$1 < PW < 11$ mm	PW = 6 mm $\omega = -3.6$ hPa/h	PW = 7 mm $\omega = -5.7$ hPa/h	PW = 7 mm $\omega = -8.8$ hPa/h
Moderate PW	8,590	11,533	14,504
$11 < PW < 19$ mm	PW = 15 mm $\omega = -3.8$ hPa/h	PW = 14 mm $\omega = -5.7$ hPa/h	PW = 14 mm $\omega = -9.0$ hPa/h
Large PW	14,984	11,801	7,840
$19 < PW < 65$ mm	PW = 28 mm $\omega = -3.7$ hPa/h	PW = 28 mm $\omega = -5.6$ hPa/h	PW = 27 mm $\omega = -8.5$ hPa/h

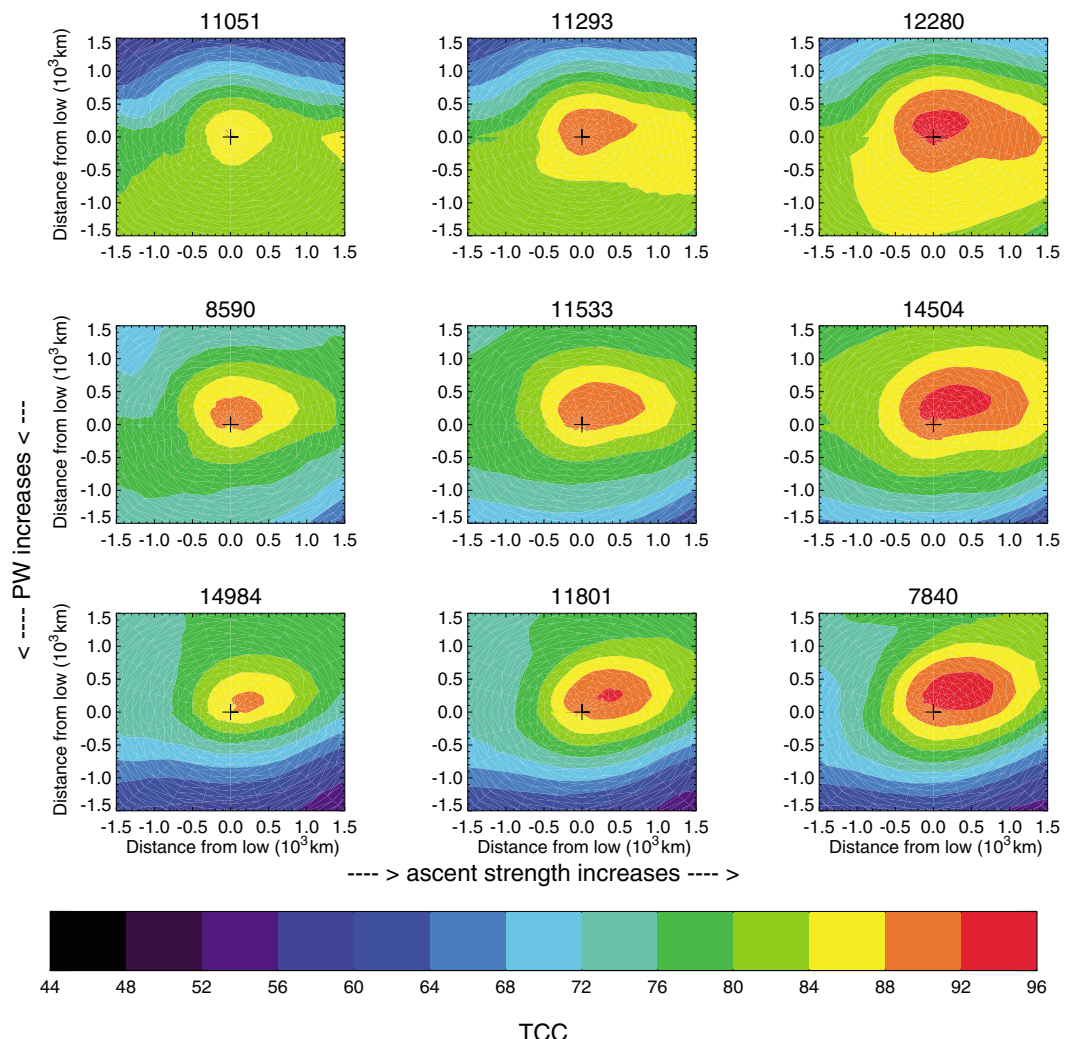


**Figure 5.** Cyclone-centered composites of MODIS total cloud cover (TCC) for nine MERRA-2 PW-ascent strength-defined categories: From left to right ascent strength increases and from top to bottom PW increases. The numbers at the top of each panel indicate the total number of cyclones per category. The plus sign indicates the center of the cyclones.

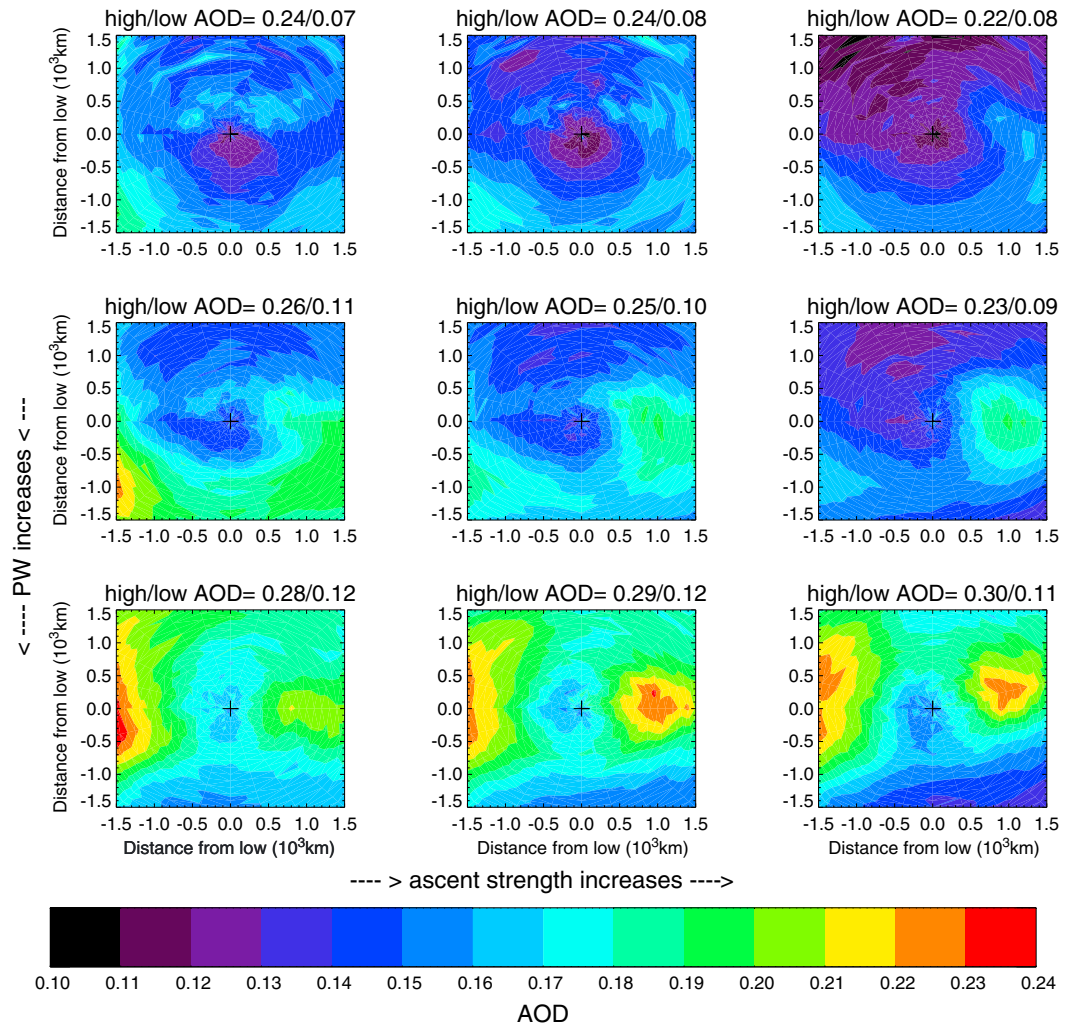


**Figure 6.** Same as Figure 5 but for MODIS AOD composites. The numbers at the top of each panel indicate the mean cyclone-wide AOD of the 30th percentile top and bottom AOD populations for each PW/ascent strength-defined category.

impact of changes in vertical velocities on changes in TCC. Consequently, we further constrain the cyclone population by PW and ascent strength conjunctly, following a method proposed by Field and Wood (2007).

### 3.2. Constraining Cyclone-Wide PW and Ascent Strength

As was done in Field and Wood (2007), and more recently in Naud and Kahn (2015), we subset the cyclones database into nine categories defined by moisture amount and cyclone strength: three categories defined by the cyclone-wide mean PW (low, moderate, and large mean PW) and three defined by the cyclone mean ascent strength (weak, moderate, and strong ascent as was done in Naud & Kahn, 2015). Because the PW/ascent strength ranges are fixed, the number of cyclones per subcategory varies, between 7,840 for the wettest and strongest cyclones and 14,984 for the wettest and weakest cyclones. Table 1 provides for each category the range of PW and ascent strength, the number of cyclones, the mean cyclone-wide PW, and the mean ascent strength.

Figure 5 shows the cyclone-centered composites of MODIS TCC for the nine categories with mean PW increasing from top to bottom and ascent strength from left to right. It is evident from this figure that dry ETCs display a minimum in cloud cover on the polar side of the center, while the wet cases display a minimum on the equator side of the center. In Naud et al. (2015), it was found that moisture increases tend to favor a transition from stratiform to convective clouds in cold frontal regions, causing a decrease in TCC as moisture

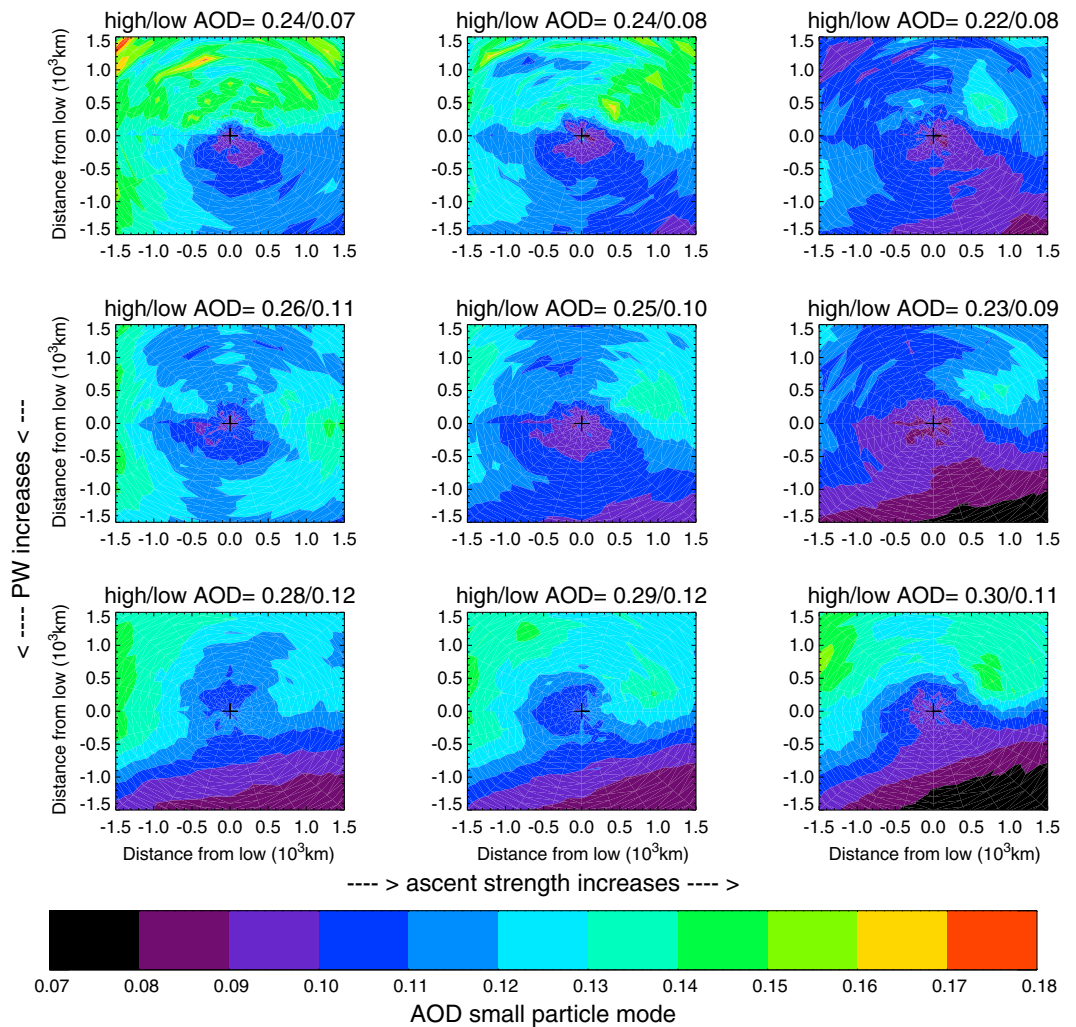


**Figure 7.** Same as Figure 6 but for the small particle mode.

increases. Figure 5 is consistent with this result. On the polar side of the cyclone, the increase in cloud cover with moisture increase is probably simply connected with a larger relative humidity in cold environments. However, we cannot rule out the fact that the MODIS cloud cover might be affected by the presence of sea ice or land in the dry cyclones (Naud et al., 2013), which are on average farther north (Naud & Kahn, 2015). The strength of the ascent impacts the total cloud cover in the warm frontal region, north and eastward of the center, as a stronger warm conveyor belt will favor cloud formation in this area of the cyclones (Field & Wood, 2007).

The distribution of AOD in the cyclones (Figure 6) does not exhibit a simple relationship with ascent strength although there is a tendency for AOD to decrease everywhere within the cyclones as ascent strength increases. The exception is a small region to the east of the low-pressure center where the change is small and the western side of the region where high PW cases show an increase (Figure 6). Previous work found a tendency for AOD to be large in areas within cyclones where surface horizontal wind speed is large, partly because changes in surface brightness impact the retrievals and also because sea salt increases with wind speed (Grandey et al., 2011). In order to examine this, we separated the MODIS AOD into the three main aerosol modes: small particle (Figure 7), sea salt like (Figure 8), and dust like (Figure 9), as in Naud, Posselt et al. (2016). MODIS retrievals of these three main aerosol modes are highly uncertain but provide a size-based classification that can be useful for numerical model constraint and evaluation. As a precaution, we use the general term sea salt-like and dust-like categories.

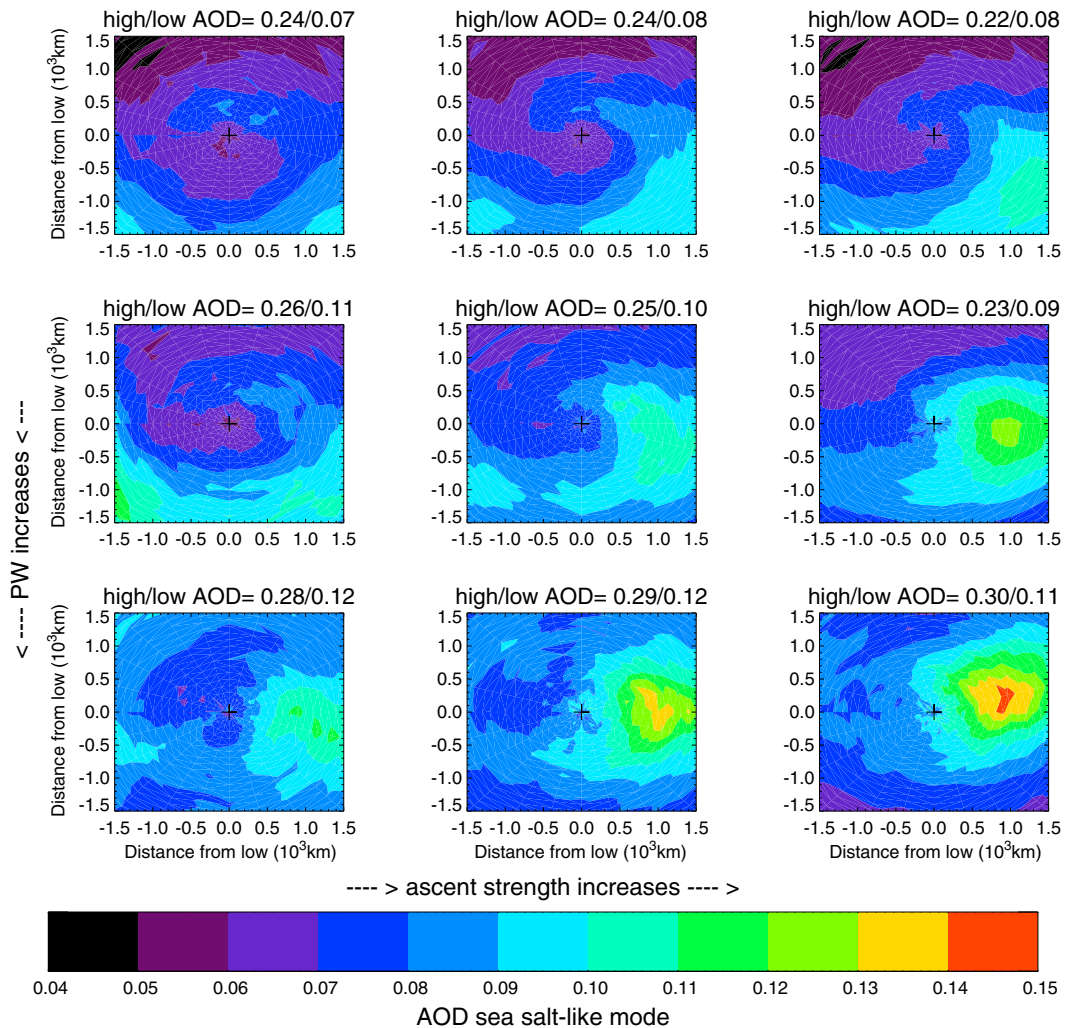


**Figure 8.** Same as Figure 6 but for the sea salt-like mode.

Results of the analysis demonstrate that we do indeed find an increase in the MODIS sea salt-like mode AOD in the warm frontal region to the east of the center as ascent strength increases (Figure 8). The dust-like AOD (Figure 9) also shows an increase with ascent strength in the equatorward half of the cyclones, which is also the region where this aerosol type might be ingested (Naud, Posselt et al. (2016)). However, the small particle AOD shows the opposite behavior at low and moderate PW: AOD decreases with ascent strength in the cold sector of the cyclones where it is maximum (Figure 7). While a number of different aerosol-cloud processes may be responsible for these trends, the observations alone cannot provide information on what processes might be at play, and we choose not to speculate on the physical relationships between changes in cyclone properties and the changes in the three categories of AOD. Such process studies should be conducted through the combined use of these observational data set, and mesoscale models in which such processes can be well represented.

The change in AOD with PW is mostly due to an increase in AOD in the two regions of the cyclones with a relative maximum. We also note a decrease in AOD on the equatorward side of the cyclone with increasing PW and an increase on the poleward side. Because aerosols tend to swell in humid conditions, it is possible that the AOD increase with PW is caused by this swelling (e.g., Jeong & Li, 2010). Also, these changes tend to follow the changes in TCC, and this might come from cloud contamination of the AOD retrievals or from multiple scattering effects (e.g., Varnai & Marshak, 2015) that can affect AOD retrievals in the vicinity of clouds (e.g., Jeong & Li, 2010; Su et al., 2008). However, when we examine each aerosol mode separately, we find again a peculiar behavior for the small particle AOD: although there is a mostly systematic decrease in

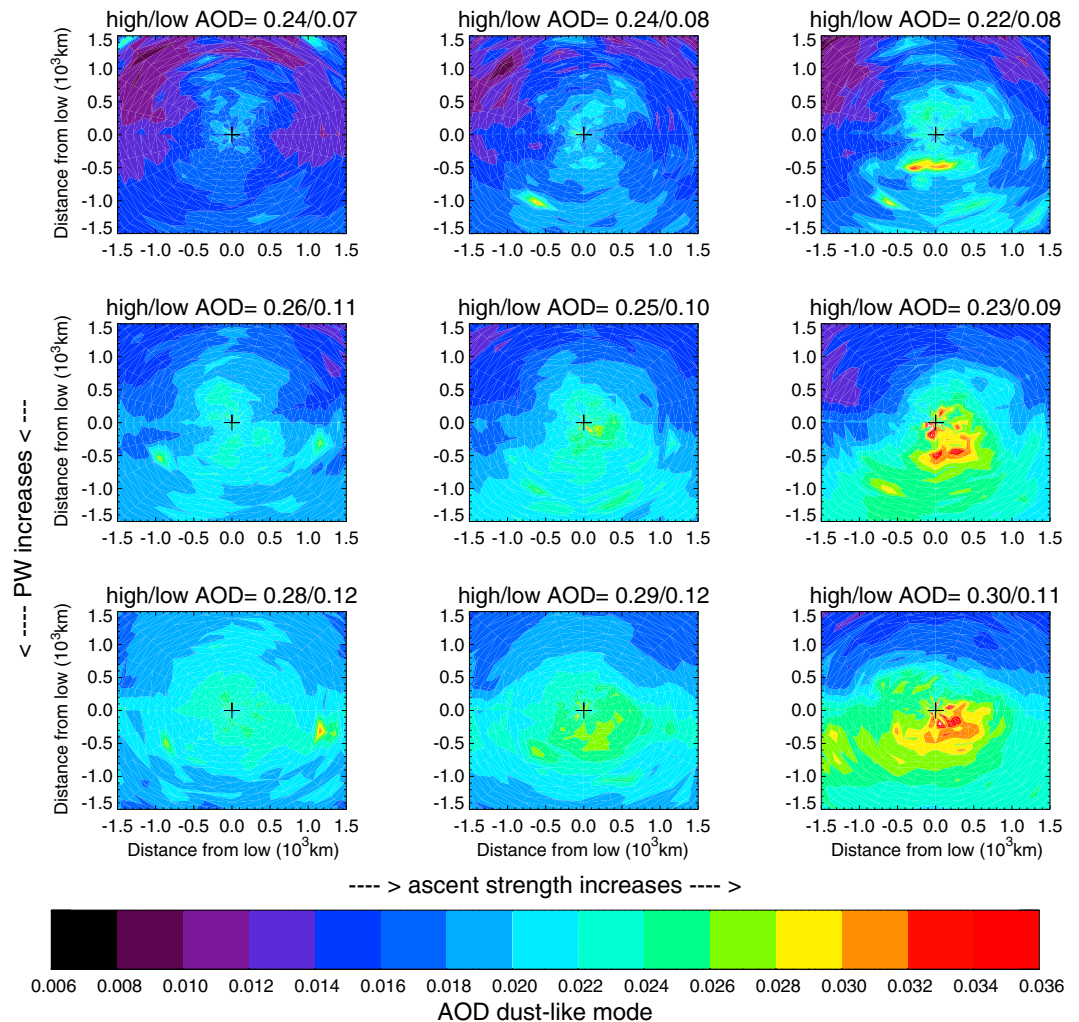


**Figure 9.** Same as Figure 6 but for the dust-like mode.

AOD with increasing PW on the equator side of the low, the polar side of the cyclone shows nonlinear variations, except for the strong ascent cases for which an increase in AOD is found for increasing PW (Figure 7). In contrast both sea salt-like and dust-like modes AOD show an increase with increasing PW everywhere in the cyclones and for all three ascent strength categories (Figures 8 and 9).

Next we further divide the nine category populations based on the cyclone-wide mean AOD into terciles and contrast the highest and lowest AOD cyclones. Figures 6–9 indicate for each PW/ $\omega$  category the mean cyclone AOD for the high and low AOD subsets. As in section 3.1, we further reduce the size of the high and low AOD populations per PW/ $\omega$  subcategory by constraining the PW distribution.

Figure 10 shows the difference in TCC ( $\Delta$ TCC) between high and low AOD cyclones for each of the nine categories. For each subcategory the contrast in PW and  $\omega$  between high and low AOD subsets is indicated, and while the change in PW is negligible, there are slight variations in the  $\omega$  change. The composites indicate a clear contrast between TCC changes on the polar side and equator side of the low. On the polar side, the TCC difference is negative, that is, cloud cover is less in high AOD cyclones than low AOD cyclones, as in Figure 4, but this difference diminishes as PW increases. On the equator side, the sign and magnitude of the TCC difference change as a function of both PW and ascent strength with a change from negative to positive as PW increases and ascent strength decreases.

The change in sign of  $\Delta$ TCC within the cyclones and across categories could be related to the change in AOD per category (Figure 6): the actual AOD per subcategory and its change between high and low AOD

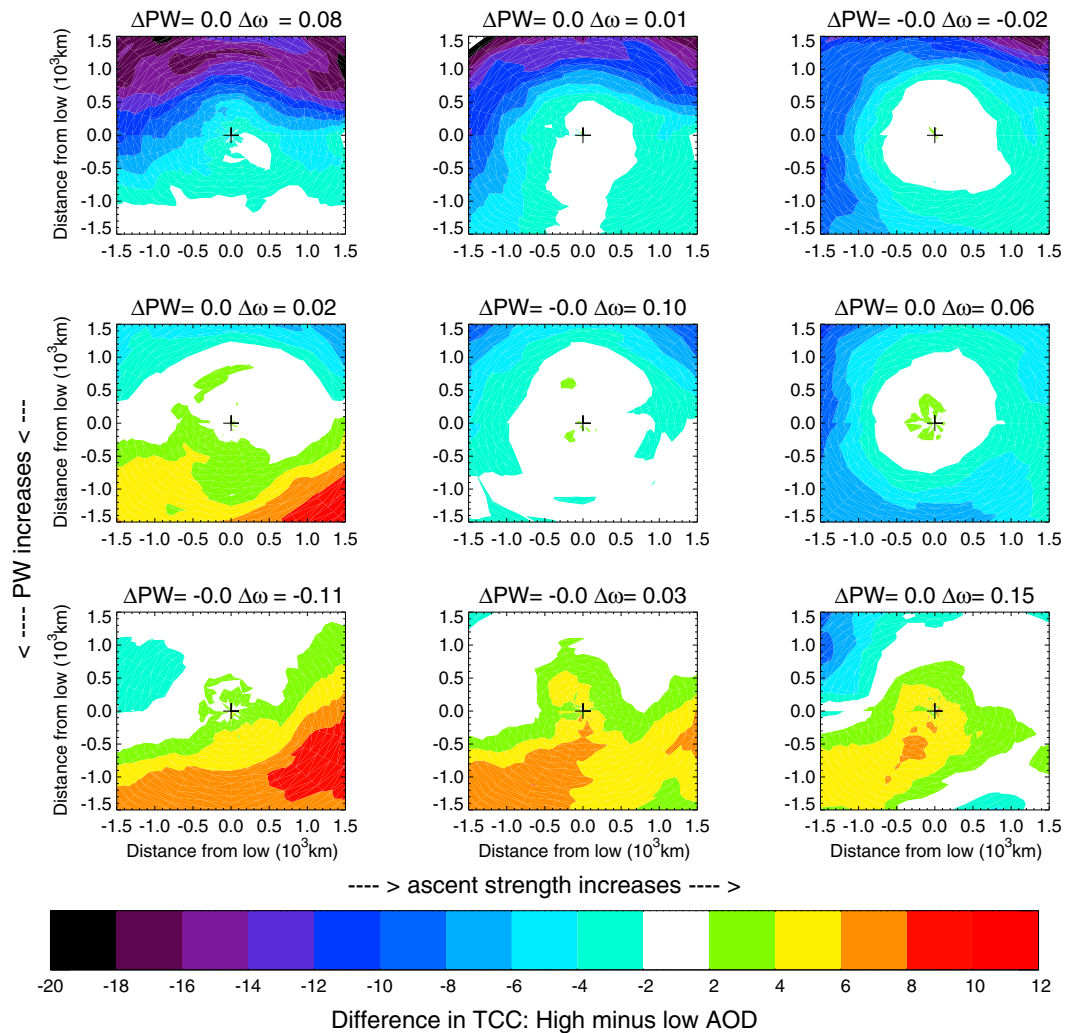


**Figure 10.** Cyclone-centered composites of the difference in MODIS TCC between high and low AOD cyclones as a function of PW (top to bottom) and ascent strength (left to right). The top of each panel indicates for each category the difference in cyclone-wide mean PW and ascent strength between the high and low AOD populations. The high and low AOD population per category were further constrained by imposing a similar cyclone-wide PW distribution.

populations slightly differ across PW/ $\omega$  categories. There might be a relation between the decrease in AOD within the cyclones and the decrease in  $\Delta\text{TCC}$  as cyclone strength increases, but the changes in  $\Delta\text{TCC}$  with cyclone-wide PW are not so clear. MODIS reports cloud cover of the highest clouds in the field of view, so if the cloud vertical distribution changes with PW (and ascent strength), Figure 10 might be showing cloud cover changes at different altitudes. This would imply that different cloud types might be affected differently by the overall aerosol concentrations in the cyclone region. Also, the frontal boundaries are not kept fixed in these composites; in particular, cold fronts move with respect to the cyclone center as cyclones age. So to get a more precise view of cloud changes, we now look at vertical transects across warm and cold fronts.

### 3.3. Cloud Cover Changes Across Frontal Boundaries Between Low and High AOD Cyclones

To examine the frontal boundaries more precisely, we turn to CloudSat-CALIPSO cloud vertical transects across warm and cold fronts. Using the same PW/ascent strength classification of cyclones as before, we collect profiles in the vicinity of cold and warm fronts when available. Consequently, the number of cases per category is less for the transects.

Figure 11 shows the composite transects across warm fronts obtained with the GEOPROF-LIDAR profiles for the nine PW-ascent strength categories. The cloud cover is maximum on the cold side of the

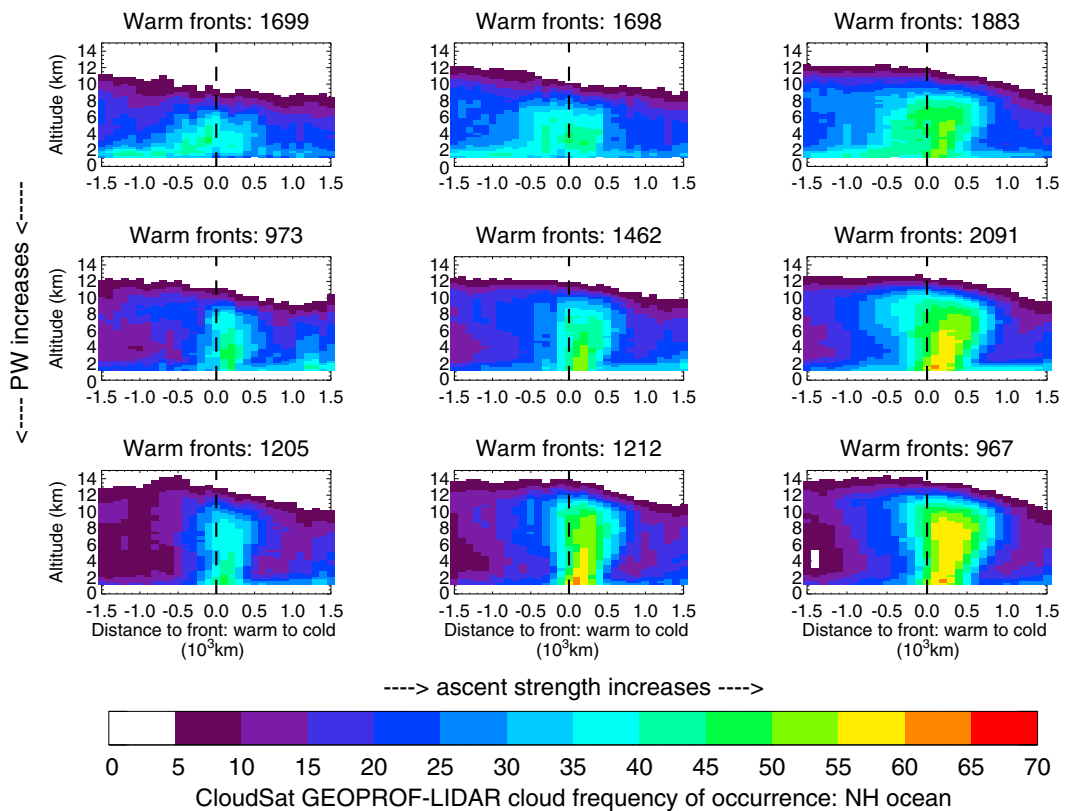


**Figure 11.** Warm front-centered vertical transects of GEOPROF-LIDAR frequency of cloud occurrence as a function of PW (top to bottom) and ascent strength (left to right) for 2006–2016 NH oceans. The numbers at the top of each panel indicate the number of fronts per composite. The dashed vertical line on each panel indicates the location of the surface front.

surface front, with clouds at all levels. North of the warm frontal maximum, low-level clouds dominate. The warm side of the front is populated mostly by high- and low-level clouds. As ascent strength increases, the amount of clouds in the warm frontal region increases and to some extent so does the low-level cloud fraction in advance of the front. As PW increases the cloud top of the frontal clouds also increases in altitude in part because the storms are found farther south, so as PW increases so does the tropopause altitude. There is also a tendency for the low-level clouds on both sides of the front to decrease as PW increases.

Figure 12 shows the composite transects across the cold fronts for the nine categories. On the cold side of the fronts low-level clouds dominate, while on the warm side of the front, clouds at all levels can be found (cf. Naud et al., 2015). As ascent strength increases, the cloud cover on the cold side of the surface front increases at low levels but seems to decrease at high levels. On the warm side of the surface front, ascent strength increases also favor an increase in all cloud levels. As noted for the warm front regions, an increase in PW seems to diminish low-level cloud cover on both sides of the front, but high-level clouds seem to increase on the cold side of the front and decrease on the warm side of the front for a given altitude. However, we note that as PW increases, so do the temperature and the tropopause height, so the decrease of cloud cover at a given altitude with increasing PW is to some extent compensated by a lifting of the clouds to higher altitudes. Going back to the MODIS change with AOD of Figure 10, the reduction in cloud cover between high and low AOD would affect mostly low-level clouds for the drier cases, but the observed increase in TCC for the wetter cases could come from changes in the high-level clouds.

Because of the limited period of time the GEOPROF-LIDAR combined product is available, we cannot further partition the nine categories into high and low AOD cyclones, as the sample size would be too small. Instead, we partition the front populations based on ascent strength and then for each of these three subcategories we impose similar PW distributions for the low and high AOD terciles (as in section 3.1).

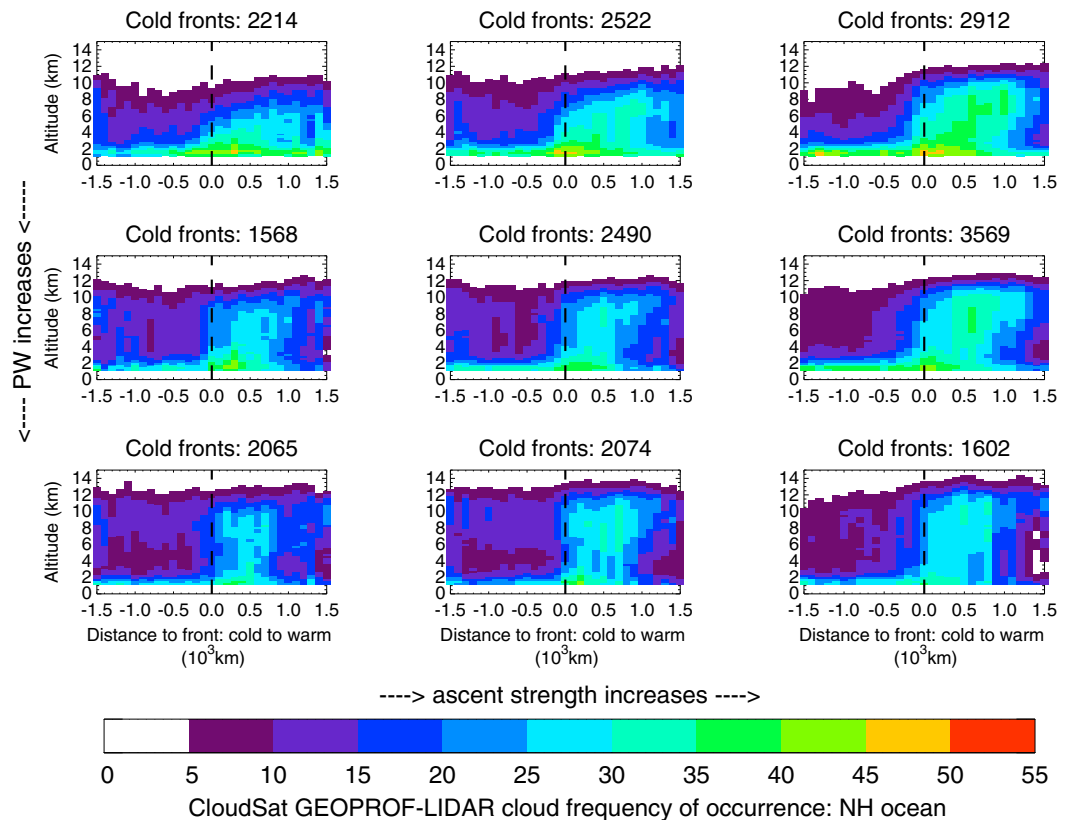


**Figure 12.** Same as Figure 11 but for cold fronts.

This was found to be a good compromise between constraining both PW and ascent strength while retaining enough data samples per AOD category.

Figure 13 shows the difference in cold and warm front transects between high and low AOD cyclones, as a function of ascent strength. For cold frontal regions (Figures 13a–13c), there is a persistent decrease in low-level clouds on the cold side of the front regardless of ascent strength. However, high-level clouds tend to increase with AOD, but this is only perceptible for the weak and moderate ascent cases (Figures 13a and 13b). On the warm side of the front, clouds above 8 km tend to occur more often in high than low AOD cases, but the signal on this side of the cold fronts is more difficult to generalize at lower levels. For warm frontal regions (Figures 13d–13f), there is a slight tendency for low-level clouds to decrease for increasing AOD on the warm side of the front but the signal is noisy. High-level clouds also increase with AOD on this side of the front, but close to the front itself the opposite is true for middle-level clouds and weak or moderate ascent. On the cold side of the warm fronts there is a large increase in low- and middle-level clouds in the region of maximum cloud cover within about 500 km north of the surface front with increasing AOD. This increase extends vertically and away from the front for strong ascent cases, suggesting perhaps a change in the tilt of the frontal cloud region. These observations are relatively consistent with previous cloud-resolving model simulations of changes in warm frontal clouds with AOD changes (Igel et al., 2013).

When comparing these transects to the differences in MODIS cloud cover (Figure 10), some behaviors are consistent: on the equator side of the low, across the cold frontal region, it seems that high AOD cyclones have less low-level clouds but more high-level clouds than low AOD cyclones, and these changes compensate one another depending on the strength of the ascent and the amount of moisture in the cyclones. Results in the warm frontal regions are more difficult to reconcile with the MODIS plan view: either the highest clouds in the scene are not changing and thus masking the MODIS top view changes at low levels as seen with CloudSat-CALIPSO or the changes of Figures 13d–13f are affected by sample size.

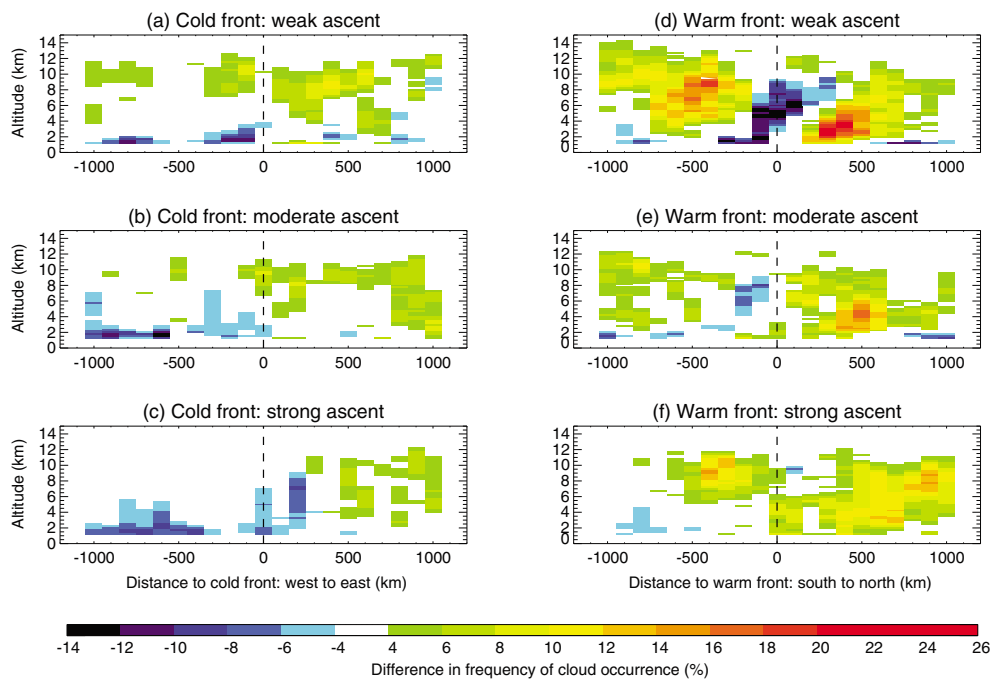


**Figure 13.** Difference in vertical distribution of GEOPROF-LIDAR cloud frequency of occurrence across cold and warm front between high and low AOD cyclones, as a function of ascent strength: (a, d) weak ascent, (b, e) moderate ascent, and (c, f) strong ascent. The cyclone-wide PW distribution is constrained so it is similar in both low and high AOD populations. The x axis gives the distance to the front, from west to east for cold fronts and south to north for warm fronts. The vertical dashed lines represent the location of the surface front.

Based on the observations at our disposal, there is a strong indication that high AOD cyclones tend to have lower cloud cover at lower levels in the cold sector than their low AOD counterparts, and when present, more high- and middle-level clouds. With maybe less certainty, the observations also suggest larger cloud cover at middle and high levels in the warm sector of the cyclones. Based on our previous study (Naud, Posselt et al., 2016), MODIS-retrieved small particle mode AOD dominates in the cold sector of the Northern Hemisphere ocean cyclones, while sea salt-like and dust-like aerosol modes are more prominent in the warm sector. This would suggest that small particles are ingested and affect clouds in the cold sector boundary layer, while dust might be more readily lofted in the warm conveyor belt and thus affecting middle- and high-level clouds. However, model simulations would be needed at this point to investigate the impact these different types of aerosols might have on the different cloud levels. Such work is currently being pursued in which the impacts of aerosols on the cloud and precipitation characteristics of postcold frontal boundary layer clouds are being investigated, as is the transport efficiency of aerosols throughout the entire ETC storm system.

#### 4. Conclusions

In this study, we have examined how total cloud cover and aerosol optical depth covary in extratropical cyclones using MODIS-Aqua, CloudSat, and CALIPSO observations. We focus on the Northern Hemisphere oceans where variability in AOD is large (Naud, Posselt et al., 2016) and use cyclone-centered composites of MODIS AOD, MODIS total cloud cover, MERRA-2 PW, and vertical velocities at 500 hPa. When contrasting the highest and lowest terciles of cyclone-wide mean AOD, we impose the constraint that the mean cyclone-wide PW distribution in these two terciles is identical. This constraint is designed to reduce the impact of PW on both AOD and cloud cover. We then find that the AOD differences are largest in the southwest quadrant of the cyclone. Total cloud cover on the equatorward side of the low is similar for low and high AOD storms, while it is lower on the polar edge of the cyclone region in high versus low AOD cyclones. High AOD cyclones are on average weaker than their low AOD counterparts (based on the 500 hPa vertical

velocity), and this suggests that the observed differences in cloud cover could be related to dynamical differences (possibly caused by aerosol impacts on the dynamics) rather than directly related to differing aerosol concentrations.

Consequently, we examine the impact of PW and ascent strength on both cloud cover and AOD by sorting the cyclones into nine categories: three PW ranges from low to high times three ascent strength categories from weak to strong. In an effort to facilitate model evaluation and constraint, we show how total cloud cover, total AOD, and AOD for each of the three main aerosol modes (small particle, sea salt like, and dust like) change when both PW and ascent strength change. Then we partition these subcategories again based on the mean cyclone-wide AOD and examine the difference in total cloud cover between the highest and lowest AOD cyclones terciles. As an additional constraint, we impose similar cyclone-wide PW distributions in these AOD-based terciles. We find that the changes in total cloud cover between high AOD and low AOD cyclones depend on how humid and how strong the cyclones are: total cloud cover is less in high AOD than low AOD cyclones when these are dry and/or strong, but it is larger in high than low AOD cyclones when these are wet and/or weak. By compositing CloudSat-CALIPSO cloud cover profiles across warm and cold front, we find that these results might be caused by differences in cloud vertical distribution between wet and dry cyclones: the covariation between cloud cover and AOD for low-level clouds is overall a decrease in cloud cover in the cold sector of the cyclones and an increase in cloud cover in the warm sector of the cyclones as AOD increases. However, high-level clouds are more widespread in more humid cyclones, and the cloud cover of the high clouds increases when AOD increases, thus masking low-level cloud changes when using MODIS observations. Changes across cold fronts are much more independent of cyclone strength, and to some extent PW, than are the changes across warm fronts. In other words, extratropical cyclones in high AOD environments tend to have greater middle- and high-level cloud cover but smaller low-level cloud cover than ETCS in low AOD environments, and these changes are modulated by the environmental humidity.

Overall, the observations highlight the strong impact of moisture amounts and cyclone dynamics on cloud cover, and possibly aerosol optical depth retrievals, in extratropical cyclones. They also illustrate how moisture and dynamics can mask, at least to some extent, possible relationships between aerosol amounts and cloud cover. In addition, the lack of AOD retrievals in cloudy conditions prevents any definite conclusions regarding causal relations between aerosols and cloud cover or any quantitative description of their covariance in the cyclones. Furthermore, cloud-aerosol interaction processes cannot be observed with the data sets at our disposal. This said, the results shown here offer information on the cyclone aerosol environment and how AOD may covary with cloud amount at various levels. They also offer constraint on modeling efforts and can be compared to numerical sensitivity studies of the impact of aerosols on simulated cyclones. The observations suggest that aerosols in the cyclone environment may suppress cloud cover at low levels but enhance cloud cover at high levels. In addition, observations in the drier cyclones offer more robust relationships between cloud cover and AOD as they avoid the issue of aerosol swelling in humid conditions, which can lead to overestimated AOD. Finally, these observations also suggest that aerosol impacts are modulated by environmental conditions not dissimilar to what is found in mesoscale convective systems (Grant & van den Heever, 2015; Khain et al., 2008; Storer et al., 2014, 2010). However, a more detailed examination of the impact of aerosols on cloud cover and the processes responsible would require examination with high-resolution simulations.

Finally, one important missing piece in our study is how precipitation might relate to AODs and cloud cover through wet scavenging. With the advent of the NASA Global Precipitation Measurement mission (Hou et al., 2014), an approach similar to this one could be used to include this important parameter but not until the mission has provided a sufficiently large sample of precipitation in cyclones. This will be an aspect we intend to explore further in the near future.

## References

- Ackerman, S. A., Holz, R. E., Frey, R., Eloranta, E. W., Maddux, B. C., & McGill, M. (2008). Cloud detection with MODIS. Part II: Validation. *Journal of Atmospheric and Oceanic Technology*, 25, 1073–1086.
- Bauer, M., & Del Genio, A. D. (2006). Composite analysis of winter cyclones in a GCM: Influence on climatological humidity. *Journal of Climate*, 19, 1652–1672.
- Bauer, M. P., Tselioudis, G., & Rossow, W. B. (2016). A new climatology for investigating storm influences in and on the extratropics. *Journal of Applied Meteorology and Climatology*, 55, 1287–1303.

## Acknowledgments

Funding for this study comes from NASA CloudSat science team recompete grant NNX13AQ33G. The MCMS extratropical cyclone data set, algorithm, and documentation are available at <http://gcss-dime.giss.nasa.gov/mcms/>. The MODIS Aqua collection 6 daily MYD08\_D3 files were obtained from the Level 1 and Atmosphere Archive and Distribution system at the Goddard Space Flight <https://ladsweb.nascom.nasa.gov>. The CloudSat-CALIPSO joint products were obtained from the CloudSat Data Processing Center <http://www.cloudsat.cira.colostate.edu/>. MERRA-2 files were obtained from the NASA Goddard Earth Sciences Data and Information Services Center. A portion of this research was carried out at the Jet Propulsion Laboratory, California Institute of Technology, under a contract with the National Aeronautics and Space Administration. We are grateful to three anonymous reviewers whose suggestions and comments helped significantly improve this manuscript.

- Bengtsson, L., Hodges, K. I., & Keenlyside, N. (2009). Will extratropical storms intensify in a warmer climate? *Journal of Climate*, 22, 2276–2301.
- Catto, J. L., Jakob, C., Berry, G., & Nicholls, N. (2012). Relating global precipitation to atmospheric fronts. *Geophysical Research Letters*, 39, L10805. <https://doi.org/10.1029/2012GL051736>
- Catto, J. L., Shaffrey, L. C., & Hodges, K. I. (2011). Northern hemisphere extratropical cyclones in a warming climate in the HiGEM high-resolution climate model. *Journal of Climate*, 24, 5336–5352.
- Dee, D. P., Uppala, S., Simmons, A., Berrisford, P., Poli, P., Kobayashi, S., ... Vitart, F. (2011). The ERA-Interim reanalysis: Configuration and performance of the data assimilation systems. *Quarterly Journal of the Royal Meteorological Society*, 137, 553–597.
- Field, P. R., & Wood, R. (2007). Precipitation and cloud structure in midlatitude cyclones. *Journal of Climate*, 20, 233–254.
- Fromm, M., Kablitz, G. III, & Caffrey, P. (2016). Dust-infused baroclinic cyclone storm clouds: The evidence, meteorology and some implications. *Geophysical Research Letters*, 43, 12,643–12,650. <https://doi.org/10.1002/2016GL071801>
- Gelaro, R., McCarty, W., Suárez, M. J., Todling, R., Molod, A., Takacs, L., ... Zhao, B. (2017). The Modern-Era Retrospective Analysis for research and Applications, version 2 (MERRA-2). *Journal of Climate*, 30, 5419–5454. <https://doi.org/10.1175/JCLI-D-16-0758.1>
- Grandey, B. S., Stier, P., Wagner, T. M., Grainger, R. G., & Hodges, K. I. (2011). The effect of extratropical cyclones on satellite-retrieved aerosol properties over ocean. *Geophysical Research Letters*, 38, L13805. <https://doi.org/10.1029/2011GL047703>
- Grant, L. D., & van den Heever, S. C. (2015). Cold pool and precipitation responses to aerosol loading: Modulation by dry layers. *Journal of the Atmospheric Sciences*, 72, 1398–1408.
- Haynes, J. M., Jakob, C., Rossow, W. B., Tseliouidis, G., & Brown, J. (2011). Major characteristics of Southern Ocean cloud regimes and their effects on the energy budget. *Journal of Climate*, 24, 5061–5080. <https://doi.org/10.1175/2011JCLI4052.1>
- Hewson, T. D. (1998). Objective fronts. *Meteorological Applications*, 5, 37–65.
- Hou, A. Y., Kakar, R. K., Neeck, S., Azbarzin, A. A., Kummerow, C. D., Kojima, M., ... Iguchi, T. (2014). The global precipitation measurement mission. *Bulletin of the American Meteorological Society*, 95, 701–722. <https://doi.org/10.1175/BAMS-D-13-00164.1>
- Igel, A. L., van den Heever, S. C., Naud, C. M., Saleeby, S. M., & Posselt, D. J. (2013). Sensitivity of warm frontal processes to cloud-nucleating aerosol concentrations. *Journal of the Atmospheric Sciences*, 70, 1768–1783.
- Jeong, M.-J., & Li, Z. (2010). Separating real and apparent effects of cloud, humidity and dynamics on aerosol optical thickness near cloud edges. *Journal of Geophysical Research*, 115, D00K32. <https://doi.org/10.1029/2009JD013547>
- Joos, H., Madonna, E., Witlox, K., Ferrachat, S., Wernli, H., & Lohmann, U. (2017). Effect of anthropogenic aerosol emissions on precipitation in warm conveyor belts in the western North Pacific in winter—A model study with ECHAM6-HAM. *Atmospheric Chemistry and Physics*, 17, 6243–6255. <https://doi.org/10.5194/acp-17-6243-2017>
- Khain, A. P., BenMoshe, N., & Pokrovsky, A. (2008). Factors determining the impact of aerosols on surface precipitation from clouds: An attempt at classification. *Journal of the Atmospheric Sciences*, 65, 1721–1748.
- Lau, N.-C., & Crane, M. W. (1995). A satellite view of the synoptic-scale organization of cloud properties in midlatitude and tropical circulation systems. *Monthly Weather Review*, 123, 1984–2006.
- Levy, R. C., Mattoo, S., Munchak, L. A., Remer, L. A., Sayer, A. M., Padadia, F., & Hsu, N. C. (2013). The collection 6 MODIS aerosol products over land and ocean. *Atmospheric Measurement Techniques*, 6, 2989–3034. <https://doi.org/10.5194/amt-6-2989-2013>
- Levy, R. C., Remer, L. A., Tanré, D., Kaufman, Y. J., Ichoku, C., Holben, B. N., ... Maring, H. (2003). Evaluation of the Moderate-Resolution Imaging Spectroradiometer (MODIS) retrievals of dust aerosol over the ocean during PRIDE. *Journal of Geophysical Research*, 108(D19), 8594. <https://doi.org/10.1029/2002JD002460>
- Li, M., Woollings, T., Hodges, K., & Masato, G. (2014). Extratropical cyclones in a warmer, moister climate: A recent Atlantic analogue. *Geophysical Research Letters*, 41, 8594–8601. <https://doi.org/10.1002/2014GL062186>
- Mace, G. G., & Zhang, Q. (2014). The CloudSat radar-lidar geometrical profile product (RL-GeoProf): Updates, improvements, and selected results. *Journal of Geophysical Research – Atmospheres*, 119, 9441–9462. <https://doi.org/10.1002/2013JD021374>
- Menzel, W. P., Frey, R. A., Zhang, H., Wylie, D. P., Moeller, C. C., Holz, R. E., ... Gumley, L. E. (2008). MODIS global cloud-top pressure and amount estimation: Algorithm description and results. *Journal of Applied Meteorology and Climatology*, 47, 1175–1198.
- Naud, C. M., & Kahn, B. H. (2015). Thermodynamic phase and ice cloud properties in the northern hemisphere winter extratropical cyclones observed by Aqua AIRS. *Journal of Applied Meteorology and Climatology*, 54, 2283–2303. <https://doi.org/10.1175/JAMC-D-15-0045.1>
- Naud, C. M., Booth, J. F., & Del Genio, A. D. (2016). The relationship between boundary layer stability and cloud cover in the post-cold-frontal region. *Journal of Climate*, 29, 8129–8149. <https://doi.org/10.1175/JCLI-D-15-0700.1>
- Naud, C. M., Booth, J. F., Posselt, D. J., & van den Heever, S. C. (2013). Multiple satellite observations of cloud cover in extratropical cyclones. *Journal of Geophysical Research*, 118, 9982–9996. <https://doi.org/10.1002/jgrd.50718>
- Naud, C. M., Del Genio, A. D., & Bauer, M. (2006). Observational constraints on the cloud thermodynamic phase in midlatitude storms. *Journal of Climate*, 19, 5273–5288.
- Naud, C. M., Del Genio, A. D., Bauer, M., & Kovari, W. (2010). Cloud vertical distribution across warm and cold fronts in CloudSat-CALIPSO data and a general circulation model. *Journal of Climate*, 23, 3397–3415.
- Naud, C. M., Posselt, D. J., & van den Heever, S. C. (2012). Observational analysis of cloud and precipitation in midlatitude cyclones: Northern versus Southern Hemisphere warm fronts. *Journal of Climate*, 25, 5135–5151.
- Naud, C. M., Posselt, D. J., & van den Heever, S. C. (2015). A CloudSat-CALIPSO view of cloud and precipitation properties across cold fronts over the global oceans. *Journal of Climate*, 28, 6743–6762.
- Naud, C. M., Posselt, D. J., & van den Heever, S. C. (2016). Aerosol optical depth distribution in extratropical cyclones over the northern hemisphere oceans. *Geophysical Research Letters*, 43, 10,504–10,511. <https://doi.org/10.1002/2016GL070953>
- Neu, U., Akperov, M. G., Bellenbaum, N., Benestad, R., Blender, R., Caballero, R., ... Wernli, H. (2013). IMILAST—a community effort to intercompare extratropical cyclone detection and tracking algorithms. *Bulletin of the American Meteorological Society*, 94, 529–547. <https://doi.org/10.1175/BAMS-D-11-00154.2>
- Pfahl, S., & Sprenger, M. (2016). On the relationship between extratropical cyclone precipitation and intensity. *Geophysical Research Letters*, 43, 1752–1758. <https://doi.org/10.1002/2016GL068018>
- Remer, L. A., Kaufman, Y. J., Tanré, D., Mattoo, S., Chu, D. A., Martins, J. V., ... Holben, B. N. (2005). The MODIS aerosol algorithm, products, and validation. *Journal of the Atmospheric Sciences*, 62, 947–973.
- Rosenfeld, D., Andreae, M. O., Asmi, A., Chin, M., de Leeuw, G., Donovan, D. P., ... Quaas, J. (2014). Global observations of aerosol-cloud-precipitation-climate interactions. *Reviews of Geophysics*, 52, 750–808. <https://doi.org/10.1002/2013RG000441>
- Salomonson, V. V., Barnes, W. L., Maymon, P. W., Montgomery, H. E., & Ostrow, H. (1989). MODIS: Advanced facility instrument for studies of the Earth as a system. *IEEE Transactions on Geoscience and Remote Sensing*, 27, 145–153.
- Simmonds, I., Keay, K., & Bye, J. A. T. (2012). Identification and climatology of Southern Hemisphere mobile fronts in a modern reanalysis. *Journal of Climate*, 25, 1945–1962.

- Stephens, G. L., Vane, D. G., Boain, R. J., Mace, G. G., Sassen, K., Wang, Z., ... the CloudSat Science Team, the CloudSat Science Team (2002). The CloudSat mission and the A-TRAIN: A new dimension to space-based observations of clouds and precipitation. *Bulletin of the American Meteorological Society*, 83, 1771–1790.
- Storer, R. L., van den Heever, S. C., & LeCuyer, T. S. (2014). Observations of aerosol-induced convective invigoration in the tropical East Atlantic. *Journal of Geophysical Research*, 119, 3963–3975. <https://doi.org/10.1002/2013JD020272>
- Storer, R. L., van den Heever, S. C., & Stephens, G. L. (2010). Modeling aerosol impacts on convective storms in different environments. *Journal of the Atmospheric Sciences*, 67, 3904–3915.
- Su, W., Schuster, G. L., Loeb, N. G., Rogers, R. R., Ferrare, R. A., Hostetler, C. A., ... Orlund, M. D. (2008). Aerosol and cloud interaction observed from high spectral lidar data. *Journal of Geophysical Research*, 113, D24202. <https://doi.org/10.1029/2008JD010588>
- Tselioudis, G., Zhang, Y., & Rossow, W. B. (2000). Cloud and radiation variations associated with northern midlatitude low and high sea level pressure regimes. *Journal of Climate*, 13, 312–327.
- Varnai, T., & Marshak, A. (2015). Effect of cloud fraction on near-cloud aerosol behavior in the MODIS atmospheric correction ocean color product. *Remote Sensing*, 7, 5283–5299. <https://doi.org/10.3390/rs70505283>
- Wang, Y., Wang, M., Xhang, R., Ghan, S. J., Lin, Y., Hu, J., ... Molina, M. J. (2014). Assessing the effects of anthropogenic aerosols on Pacific storm track using a multiscale global climate model. *Proceedings of the National Academy of Sciences*, 111, 6894–6899. <https://doi.org/10.1073/pnas.1403364111>
- Wang, Y., Zhang, R., & Saravanan, R. (2014). Asian pollution climatically modulates mid-latitude cyclones following hierarchical modelling and observational analysis. *Nature Communications*, 5, 3098. <https://doi.org/10.1038/ncomms4098>
- Winker, D. M., Vaughan, M. A., Omar, A. H., Hu, Y., Powell, K. A., Liu, Z., ... Young, S. A. (2009). Overview of the CALIPSO mission and CALIOP data processing algorithms. *Journal of Atmospheric and Oceanic Technology*, 26, 2310–2323.
- Yetella, V., & Kay, J. (2016). How will precipitation change in extratropical cyclones as the planet warms? Insights from a large initial condition climate model ensemble. *Climate Dynamics*. <https://doi.org/10.1007/s00382-016-3410-2>
- Zhang, R., Li, G., Fan, J., Wu, D. L., & Molina, M. J. (2007). Intensification of Pacific storm track linked to Asian pollution. *Proceedings of the National Academy of Sciences of the United States of America*, 104(13), 5295–5299. <https://doi.org/10.1073/pnas.0700618104>